Exp Fluids (2017) 58:56
DOI 10.1007/s00348-017-2344-8

RESEARCH ARTICLE

Dynamic mode decomposition for estimating vortices and lee waves in a stratified wake

Xinjiang Xiang[1] · **Kevin K. Chen**[2] · **Geoffrey R. Spedding**[1]

Received: 27 October 2016 / Accepted: 7 April 2017 / Published online: 11 April 2017

Abstract Dynamic mode decomposition (DMD) is an analysis technique for extracting flow patterns and their dynamics from experimental or simulated velocity fields. Here, DMD is applied to experimental data in the vertical center-plane of wakes generated by a towed grid in a stably stratified background, at varying values of the dimensionless Froude and Reynolds Number. The primary goal was to identify dynamically important patterns and reveal the influence of stratification on their initiation and evolution. It is demonstrated that DMD captures lee wave and vortical modes with different length scales successfully. Further, one can construct a mode energy spectrum which shows a clear dependence on Froude Number, with energy transfer to larger scales in the near wake, as the initial shear-triggered Kelvin–Helmholtz roll-ups diffuse and pair with neighbors. Finally, this paper serves as a detailed example of the application of DMD to time-resolved particle imaging velocimetry data for a stratified flow. The results confirm its utility in objective identification of dynamics at different scales of complex fluid flows.

1 Introduction

Since the evolution of a wake in a stable background density gradient is restricted by stratification, the dynamics differ significantly from its counterpart in a homogeneous ambient. Regardless of the initial degree of turbulent kinetic energy, such wakes eventually evolve into a state dominated by low Froude number dynamics with persistent patterns and, therefore, are of special interest to both predictive geophysical studies and potential signal/pattern detectors (Spedding 2014).

Overall, a simple 3-stage model [3D-NEQ-Q2D; Spedding (1997)] can satisfactorily account for a number of late wake characteristics, and various modifications have been proposed to include experimental (Bonnier and Eiff 2002) and theoretical (Meunier et al. 2006) considerations. Though the experimental fits seem effective, the theoretical model does not scale in the same way with Froude number, and there is some dispute about how and whether these mechanisms could be universal, and when and if the evolution could be independent of initial conditions. For example, in columnar vortex pairs, zigzag modes drive the transition to vertical layering (Billant and Chomaz 2000) with set vertical length scales (Billant 2010; Billant et al. 2010). However, when the initial state is turbulent, there is no initial coherence in vertical direction. Pattern and structure in the horizontal or isopycnal plane behind both streamlined and bluff bodies can be traced to KH-type pairing–merging mechanisms (Spedding 2001, 2002).

In many geophysical flows, with characteristic length and velocity scales, L and U, the Reynolds number $\mathrm{Re} = UL/\nu$ characterizes the relative timescales associated with inertial-scale and viscous-scale events, and an internal Froude number $\mathrm{Fr} = U/NL$ characterizes advective vs. buoyancy timescales (the buoyancy frequency N is the natural oscillation frequency due to background density variation). Since L on the scale of geography is large, it is common for $\mathrm{Re} \sim 10^8$, while $\mathrm{Fr} = O(1)$, which immediately tells us two things: (1) stratification is always important in the free evolution of L-scale disturbances; (2)

✉ Xinjiang Xiang
xinjianx@usc.edu

[1] University of Southern California, Los Angeles, CA 90089, USA

[2] Institute for Defense Analysis, Center for Communication Research-La Jolla, San Diego, CA 92121, USA

at least at first, while Re remains high, then the dynamical regime will be one in which buoyancy is influential and at the same time viscosity is not. This strongly-stratified turbulent regime is sometimes described by a buoyancy-Reynolds number, $Re_b \sim Re \cdot Fr^2$, and when $Re_b >> 1$ one expects and observes that non-equilibrium conditions last significantly longer (Meunier et al. 2006; Diamessis et al. 2011), and the driving dynamics of the inertial-driven but buoyancy-controlled flows are more complex than in viscous-controlled motions (Riley and de Bruyn Kops 2003; Hebert and de Bruyn Kops 2006).

Two limitations are driving experimental studies to earlier times in stratified turbulence evolution. There is some natural limit in L in any facility, and so turbulence must be associated with large U. There is also a limit on maximum N and conditions of high-U, high-N (and hence low Fr) can be found only in early evolution times, when the flow is strongly three-dimensional. In fact the existence of the notional 3D stage, where the dynamics at some range of scales occurs mostly unaffected by ambient stratification, has been largely a matter of conjecture because strong variations in the density fields make measurement by optical-based methods difficult.

Recent experiments in a refractive index matched fluid (Xiang et al. 2015) have provided measurements of the near wake of localized grid turbulence over the 3D to NEQ transition in a turbulent wake, as have direct numerical simulations for sphere wakes (Orr et al. 2015), and it is now possible to search for appropriate quantitative measures to describe and compare effects of initial and boundary conditions at early times, when it is quite unlikely in many instances that some universal or self-similar state will have been reached. Near wakes can be shown to exhibit a variety of flow modes whose formation depends not only on the combination of Re and Fr, but also on the body geometry or generator conditions, and a number of experiments on towed spheres have demonstrated lee waves, spiral modes, KH modes, vertical oscillation modes, and more at different Re and Fr (Lin et al. 1992; Chomaz et al. 1993). These structural components have distinct time and length scales that are related to particular physical processes, and modal analyses may be employed to isolate and decompose the near-wake field along its most energetic, or dynamically-significant modes.

Proper orthogonal decomposition (POD) is a commonly used method to compute orthogonal modes that optimally capture the vector energy of a data set and hence can efficiently extract coherent structures and may also reconstruct flow fields with a low-order representation (Holmes et al. 2012). By using physical space-based basis functions that are not necessarily time-periodic or space-filling, one can account for localized features such as turbulence patches (Lumley 2007; Berkooz et al. 1993). Some applications of POD have included stratified turbulent patches (Diamessis et al. 2010), free shear flows (Gordeyev and Thomas 2000, 2002), and boundary layer flows (Gurka et al. 2006). This method, though appealing, suffers from a certain limitations (Schmid 2010; Chen et al. 2012). First, POD may not successfully isolate flow modes with different frequencies or growth rates. Second, there is not a clear relation between the energy of a mode and its importance in the dynamics. For instance, some flows exhibit low-energy modes that trigger instabilities and are, therefore, dynamically quite important.

Dynamic mode decomposition (DMD) (Schmid 2010) is a data-based modal decomposition method that computes Koopman modes of nonlinear systems (Rowley et al. 2009) from experimental or numerical time series (Schmid 2010, 2011), where the nonlinear dynamics are fit to a linear model. An example of applying DMD to time-resolved tomographic PIV data is provided by Schmid et al. (2012). DMD yields modes that have physically meaningful growth rates and frequencies given by the magnitude and phase of corresponding discrete-time eigenvalues. As a result, flow features with distinct frequencies can be effectively decoupled, but those without distinct patterns, as in some examples of turbulence, may not be fully characterized. In addition, growth rates describe the evolution of corresponding modes and allow the identification of unstable modes even if they have low energy in the data.

This paper applies DMD to time-resolved PIV data measured in the vertical center-plane of the near-wake generated by a towed grid in a linearly density-stratified medium. Unlike the experiments of Schmid et al. (2012), where both the flow field reference and cameras are fixed in lab reference, here the grid reference is moving with respect to the cameras, which is also the case in many wake experiments. The ultimate objective is to investigate stratification effects on the initiation and early-time evolution of different frequencies and length scales, as well as the energy transfer between them. The dynamics in this regime may then shed some light on how it is that coherent structures emerge from a (possibly turbulent) near wake.

2 Methods

2.1 Experimental methods

Experiments were conducted by horizontally towing a circular grid of radius $R = 4$ cm with square mesh spacing $M = 3.2$ mm and solidity $S = 26\%$ in a $(0.8\ \text{m})^3$ tank, as sketched in Fig. 1.

The grid orientation was maintained using tow and support wires, both attached at opposite sides of the grid so that the measurement in the vertical center-plane would not be directly disturbed at early times. The grid was towed

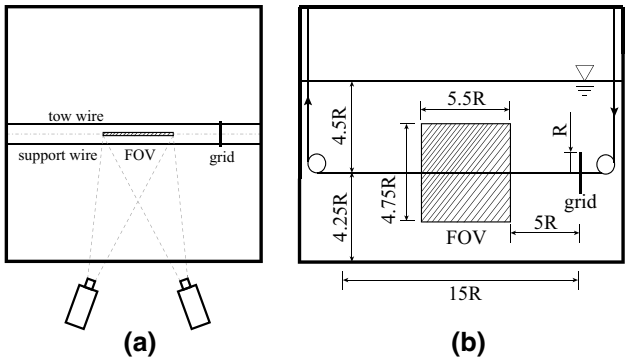

Fig. 1 Sketch of the lab experimental setup: **a** view from above; **b** view from camera side

at speeds $U = \{6.8, 14.3, 27.6\}$ cm/s through the field of view (FOV), which was of length $5.5R$ and height $4.75R$. Data collection began after a grid displacement of $5R$ to reduce transient effects. The average kinematic viscosity in the stratified wake region was $\nu \approx 1.005 \times 10^{-6}$ m^2/s, so the Reynolds numbers $\mathrm{Re} := UR/\nu$ were $\{2700, 5700, 11,000\}$. The Brunt-Väisälä frequency is defined as $N := \sqrt{(-g/\rho_0)\,(\partial\rho/\partial z)}$, where g is the gravitational acceleration, ρ_0 is a reference density, and $\partial\rho/\partial z < 0$ is the background density gradient against the direction of gravity. N ranged from 0.2 to 2.8 rad/s, so the Froude numbers $\mathrm{Fr} := U/(NR)$ were $\{0.6, 1.3, 2.4, 4.7, 9.1\}$. If one computes Re and Fr based on mesh spacing, the results will scale accordingly with a factor of 0.08.

All three components $\{u, v, w\}$ of velocity in the vertical x–z center-plane were estimated using stereoscopic PIV with a sampling rate of 20 Hz. The resolution of the measured velocity field is {32, 48, 64} pixels for Re = {2700, 5700, 11,000}, respectively. At a constant optical conversion of 11.75 pixels/mm, this yields a resolution of {2.7, 4.1, 5.4} mm for each case. To reduce optical distortions due to sharp, irregular, and time varying density gradients at early times, a refractive index matching (RIM) technique was employed as detailed in Xiang et al. (2015).

2.2 Dynamic mode decomposition

Here a practical means of computing a DMD in a time resolved PIV or simulation sequence is given. The singular value decomposition (SVD) method, presented by Schmid (2010) and further discussed by Chen et al. (2012), is followed.

Suppose a series (either temporal or spatial) of velocity fields from $m+1$ snapshots, the vector fields can be rearranged and each numerically represented by a 1D column vector $\mathbf{x}_k$ for $k = 0, \ldots, m$. DMD identifies complex Ritz values $\{\lambda_j\}_{j=1}^m$ and complex Ritz vectors $\{\mathbf{v}_j\}_{j=1}^m$ such that

$$\mathbf{x}_k = \sum_{j=1}^{m} \lambda_j^k \mathbf{v}_j, \quad k = 0, \ldots, m-1 \tag{1a}$$

$$\mathbf{x}_m = \sum_{j=1}^{m} \lambda_j^m \mathbf{v}_j + \mathbf{r}, \quad \mathbf{r} \perp \mathrm{span}\{\mathbf{x}_0, \ldots, \mathbf{x}_{m-1}\}. \tag{1b}$$

Therefore, $\mathbf{v}_j$ represents the vector of jth flow mode. The idea of performing this decomposition is to approximate the nonlinear dynamics with linear combinations of Ritz vectors $\mathbf{v}_j$; the evolution from one snapshot to the next, and the stability of each mode can be described by the magnitude and phase of Ritz values λ_j, and the residual is summarized in $\mathbf{r}$. The decomposition is unique if and only if $\{\lambda_j\}_{j=1}^m$ are distinct and $\{\mathbf{x}_k\}_{k=0}^{m-1}$ are linearly independent (Chen et al. 2012), which is usually true for evolving wakes. The first m data vectors are represented exactly by a linear combination of Ritz vectors, whereas the last data vector contains the residual vector $\mathbf{r}$ orthogonal to the span of $\{\mathbf{x}_k\}_{k=0}^{m-1}$, and is hence minimized (Rowley et al. 2009).

Below we explain the mathematical procedure to compute λ_j and $\mathbf{v}_j$. First, (1a) can be written in matrix form as

$$\mathbf{K} := \begin{bmatrix} \mathbf{x}_0 & \mathbf{x}_1 & \ldots & \mathbf{x}_{m-1} \end{bmatrix} = \mathbf{VT}, \tag{2}$$

where

$$\mathbf{V} := \begin{bmatrix} \mathbf{v}_1 & \mathbf{v}_2 & \ldots & \mathbf{v}_m \end{bmatrix} \tag{3}$$

is the eigenvector matrix and

$$\mathbf{T} := \begin{bmatrix} 1 & \lambda_1 & \lambda_1^2 & \cdots & \lambda_1^{m-1} \\ 1 & \lambda_2 & \lambda_2^2 & \cdots & \lambda_2^{m-1} \\ \vdots & \vdots & \vdots & \ddots & \vdots \\ 1 & \lambda_m & \lambda_m^2 & \cdots & \lambda_m^{m-1} \end{bmatrix} \tag{4}$$

is a Vandermonde matrix. Let $\mathbf{c} := \begin{bmatrix} c_0 & \ldots & c_{m-1} \end{bmatrix}^{\mathrm{T}}$ be the vector of coefficients that fit $\mathbf{x}_m$ to all other data vectors in a least squares sense, so that

$$\mathbf{x}_m = \mathbf{Kc} + \mathbf{r}, \quad \mathbf{r} \perp \mathrm{span}\{\mathbf{x}_0, \ldots, \mathbf{x}_{m-1}\}. \tag{5}$$

Then, the companion matrix $\mathbf{C}$ can be defined as

$$\mathbf{C} := \begin{bmatrix} 0 & 0 & \cdots & 0 & c_0 \\ 1 & 0 & \cdots & 0 & c_1 \\ 0 & 1 & \cdots & 0 & c_2 \\ \vdots & \vdots & \ddots & \vdots & \vdots \\ 0 & 0 & \cdots & 1 & c_{m-1} \end{bmatrix} \tag{6}$$

such that the index-shifted matrix $\mathbf{K}_p := \begin{bmatrix} \mathbf{x}_1 & \mathbf{x}_2 & \ldots & \mathbf{x}_m \end{bmatrix}$ is

$$\mathbf{K}_p = \mathbf{KC} + \mathbf{re}^{\mathrm{T}}, \quad \mathbf{e} := \begin{bmatrix} 0 & \ldots & 0 & 1 \end{bmatrix}^{\mathrm{T}} \tag{7}$$

The Vandermonde matrix $\mathbf{T}$ and companion matrix $\mathbf{C}$ are related in that $\mathbf{T}$ diagonalizes $\mathbf{C}$ as

$$\mathbf{C} = \mathbf{T}^{-1}\Lambda\mathbf{T}, \tag{8}$$

where Λ is a diagonal matrix with $\{\lambda_j\}_{j=1}^{m}$ on the diagonal. Hence, the eigenvalues of $\mathbf{C}$ are the Ritz values, and Ritz vectors can be recovered from (2) by $\mathbf{V} = \mathbf{K}\mathbf{T}^{-1}$.

The eigendecomposition of the companion matrix can be ill-conditioned in practice, so we employ the SVD algorithm introduced by Schmid (2010). Assume $\mathbf{K}$ is full-rank and $\mathbf{K} = \mathbf{U}\Sigma\mathbf{W}^*$ is the SVD of $\mathbf{K}$, with $(\cdot)^*$ denoting the complex conjugate. From the properties of SVD, $\mathbf{U}^*\mathbf{U} = \mathbf{I}$, and $\mathbf{W}^*\mathbf{W} = \mathbf{W}\mathbf{W}^* = \mathbf{I}$. Furthermore, since $\mathbf{K}$ and $\mathbf{U}$ span the same subspace, $\mathbf{U}^*\mathbf{r} = \mathbf{0}$. Substituting the SVD and (8) into (7), and left-multiplying by $\mathbf{U}^*$ and right-multiplying by $\mathbf{W}\Sigma^{-1}$, we obtain

$$\begin{aligned}\mathbf{U}^*\mathbf{K}_p\mathbf{W}\Sigma^{-1} &= (\Sigma\mathbf{W}^*\mathbf{T}^{-1})\Lambda(\mathbf{T}\mathbf{W}\Sigma^{-1}) \\ &= (\Sigma\mathbf{W}^*\mathbf{T}^{-1})\Lambda(\Sigma\mathbf{W}^*\mathbf{T}^{-1})^{-1}.\end{aligned} \tag{9}$$

Therefore, the Ritz values are the eigenvalues of $\mathbf{U}^*\mathbf{K}_p \cdot \mathbf{W}\Sigma^{-1}$. The reason for this step is that $\mathbf{U}$, Σ and $\mathbf{W}^*$ can be easily calculated from the data matrix $\mathbf{K}$, while $\mathbf{C}$ is unknown. Furthermore, the use of the SVD of $\mathbf{K}$ in (2) yields $\mathbf{V} = \mathbf{U}\Sigma\mathbf{W}^*\mathbf{T}^{-1}$. Denoting the eigenvector matrix $\mathbf{Y} := \Sigma\mathbf{W}^*\mathbf{T}^{-1}$, it is then apparent that $\mathbf{V} = \mathbf{U}\mathbf{Y}$. Note that when computing the eigendecomposition in (9), the eigenvectors (that is, the columns of $\mathbf{Y}$) need to be scaled appropriately so that $\mathbf{V} = \mathbf{U}\mathbf{Y}$ satisfies (2). If $\mathbf{K}$ is rank-deficient, then $\mathbf{U}$, Σ and $\mathbf{W}$ can be truncated to dimension rank($\mathbf{K}$), and the same algorithm can still be implemented to produce fewer modes (Schmid 2010).

2.3 Data reconfiguration for temporal and spatial analyses

In the experiments, the cameras are fixed in the lab reference, and the grid passes through this fixed FOV. The velocity field is, therefore, both temporally and spatially varying, so rearrangement of the data is needed for DMD calculation.

For temporal analysis, each data vector $\mathbf{x}_k$ is constructed by extracting a velocity field from half of the FOV, at a fixed x/R range in the grid reference frame, as sketched in Fig. 2 with a dashed line box. That is, suppose that the streamwise span of the FOV is LR for some L, and behind the grid the upstream extent of the velocity data is $x/R = a$ for some a (because the area behind the grid is shaded by the grid, the data are not immediately available, see Fig. 3b). We arrange the data with $x/R \in [a, a + L/2]$ column-wise into vectors

$$\mathbf{x}_0 = \begin{bmatrix} \mathbf{u}_0^{t_0} \\ \mathbf{u}_1^{t_0} \\ \mathbf{u}_2^{t_0} \\ \vdots \end{bmatrix}, \quad \mathbf{x}_1 = \begin{bmatrix} \mathbf{u}_0^{t_1} \\ \mathbf{u}_1^{t_1} \\ \mathbf{u}_2^{t_1} \\ \vdots \end{bmatrix}, \quad \mathbf{x}_2 = \begin{bmatrix} \mathbf{u}_0^{t_2} \\ \mathbf{u}_1^{t_2} \\ \mathbf{u}_2^{t_2} \\ \vdots \end{bmatrix}, \quad \cdots, \tag{10}$$

where $\mathbf{u}_i^{t_j}$ indicates a vector of velocities in the grid reference frame at time t_j at downstream distance $x/R = x_i$, with spacing $\Delta x = x_{i+1} - x_i$, as sketched in Fig. 2. In this paper x_i denotes the distance downstream of the grid, while bold $\mathbf{x}_i$ denotes the data vector, and the final data matrix $\mathbf{K}$ is constructed from $\mathbf{x}_i$ as in (2).

The matrix $\mathbf{K}$ for spatial analysis is configured slightly differently, as velocities in each $\mathbf{x}_i$ should correspond to

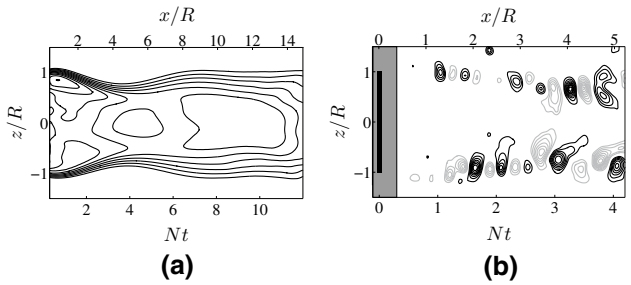

Fig. 3 The flow at Fr = 1.3, Re = 2700 in the lab reference [replotted from data originally shown in Xiang et al. (2015)]. **a** Mean streamwise velocity field $\overline{u}/U$, with minimum contour level $|c|_{\min} = 0.06$ and contour spacing $\Delta c = 0.06$. **b** Instantaneous vertical velocity field $(w - \overline{w})/|U|$, with $|c|_{\min} = 0.04$ and $\Delta c = 0.02$, and $\overline{w}$ being the mean vertical velocity. The *shaded* area is not accessible to cameras, and the *gray* contours indicate negative values

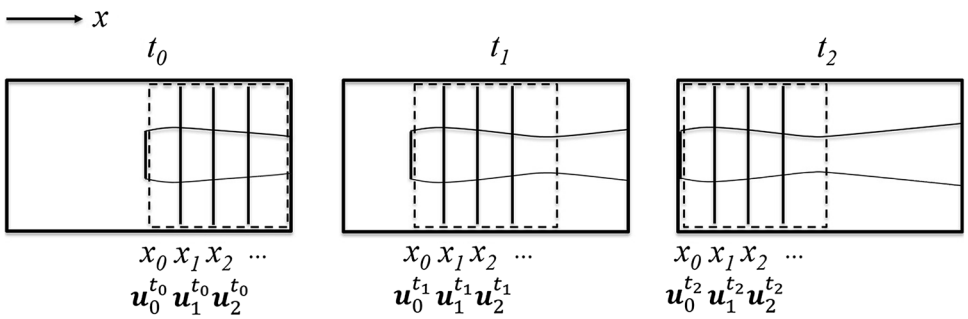

Fig. 2 Sketch of the data reconfiguration

the same x coordinate instead of time. The rearrangement can, therefore, be written as

$$\mathbf{x}_0 = \begin{bmatrix} \mathbf{u}_0^{t_0} \\ \mathbf{u}_0^{t_1} \\ \mathbf{u}_0^{t_2} \\ \vdots \end{bmatrix}, \quad \mathbf{x}_1 = \begin{bmatrix} \mathbf{u}_1^{t_0} \\ \mathbf{u}_1^{t_1} \\ \mathbf{u}_1^{t_2} \\ \vdots \end{bmatrix}, \quad \mathbf{x}_2 = \begin{bmatrix} \mathbf{u}_2^{t_0} \\ \mathbf{u}_2^{t_1} \\ \mathbf{u}_2^{t_2} \\ \vdots \end{bmatrix}, \quad \cdots. \tag{11}$$

3 Results

3.1 Wake structures

A statistical description of the grid near-wake characteristics has been given (Xiang et al. 2015), in which the most obvious features were the lee waves and Kelvin–Helmholtz (KH) billows. The lee waves are identified in the mean streamwise velocity field (Fig. 3a).

Fluid particles vertically displaced by the grid tend to restore their balanced positions, resulting in the contraction in the contour plot that moves with the grid. The dense isocontours at the wake edge also indicate strong shearing that can trigger KH instabilities, as seen in the fluctuating vertical velocity field (Fig. 3b), where bands of alternating-sign contours move at some local speed. The two-shear-layer structure in the near wake also resembles that observed in the turbulent wake of a mesh strip in homogeneous ambient (Huang and Keffer 1996).

Though these features can be visualized using statistical analysis, the quantification of the their evolution, particularly with regard to the KH modes, remains challenging and can benefit from a careful examination by DMD, where the mode extraction is systematically applied, and the evolution procedure is represented by eigenvalues.

3.2 Temporal DMD: non-oscillatory mode

In the near wake, self-similarity is neither expected nor observed, and in these stratified cases, it is also clear that a local wake height, for example, is primarily set by the lee wave, whose amplitude varies with Fr. We now investigate how the dynamics can be characterized by a temporal DMD analysis. Taking the case of Re = 2700 and Fr = 1.3 as an example, the Ritz values and scaled mode energies for a near-wake window in x are plotted in Fig. 4.

The total number of accessible modes depends on the number of independent snapshots containing the specified x/R range and is about 15 for Re = 2700, 8 for Re = 5700, and 4 for Re = 11,000 as the grid moves quickly through the FOV. Because the flow structure behind the grid is relatively simple, this number of modes is likely sufficient to capture the dominant dynamics, and the residual term $\|\mathbf{r}\|$ is only less than 2% of $\|\mathbf{x}_m\|$ for all

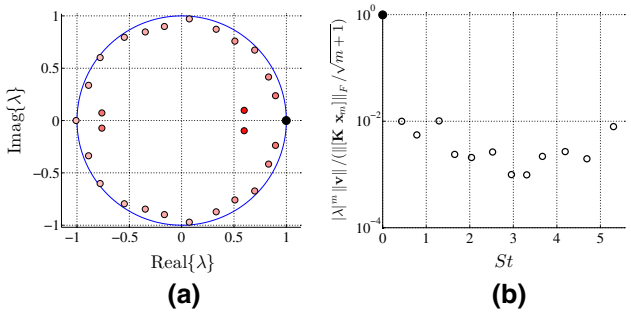

Fig. 4 **a** The Ritz values and **b** scaled mode energies for Fr = 1.3, Re = 2700, and $x/R \in [0.37, 3.04]$. *Darker color* in (**a**) indicates larger $\|\mathbf{v}\|$, with $\|\cdot\|$ denoting the l^2 norm. Modes with negative St are omitted in (**b**) as they are symmetric about the *vertical axis*. Two modes with very small energy have been omitted from (**b**). The *large solid black dot* corresponds to the first mode with St = 0

cases. The importance of a given mode is indicated by both $\|\lambda\|$ and $\|\mathbf{v}\|$, so in Fig. 4b, we plot the quantity

$$\frac{\sqrt{m+1}\,|\lambda|^m \|\mathbf{v}\|}{\|[\mathbf{K}\,\mathbf{x}_m]\|_\mathrm{F}}, \tag{12}$$

with $\|\cdot\|_\mathrm{F}$ indicating the Frobenius norm. The quantity $|\lambda|^m\|\mathbf{v}\|$ can be interpreted as the contribution of the given mode in the reconstruction of the final snapshot $\mathbf{x}_m$, which is then scaled by the average data norm $\|[\mathbf{K}\,\mathbf{x}_m]\|_\mathrm{F}/\sqrt{m+1}$. Denoting the frequency and angular speed of the jth mode by f_j and ω_j, the Strouhal number of the jth mode can be calculated from

$$\mathrm{St}_j := \frac{f_j R}{U} = \frac{\omega_j R}{2\pi U} = \frac{\mathrm{Imag}\{\ln(\lambda_j)\}R}{2\pi\,\Delta t\,U}, \tag{13}$$

where $\Delta t = 0.05$ s is the time interval between consecutive snapshots.

All modes are either almost on, or within the unit circle, as the wake is temporally neutrally stable. The mode with highest St consists of mostly random small-scale fluctuations, and its magnitude varies greatly depending on the selected x/R range and particular {Re, Fr} combination. Otherwise, it is usually the three or four modes with the lowest St that have relatively large mode energies and delineate certain near-wake flow patterns, while the higher St modes are higher-order harmonics. The mode with St = 0 is closely associated with the mean flow and dominates the reconstruction of the snapshots, containing almost 100% of the mode energy as the background flow velocity is an order of magnitude larger than the fluctuating velocities. We call it the non-oscillatory mode from here on to distinguish it from modes with non-zero frequencies.

Since DMD is conducted for data with streamwise ranges of $x/R \in [a, a+L/2], [a+L/2, a+L], \ldots$ separately, the Ritz vectors corresponding to the non-oscillatory

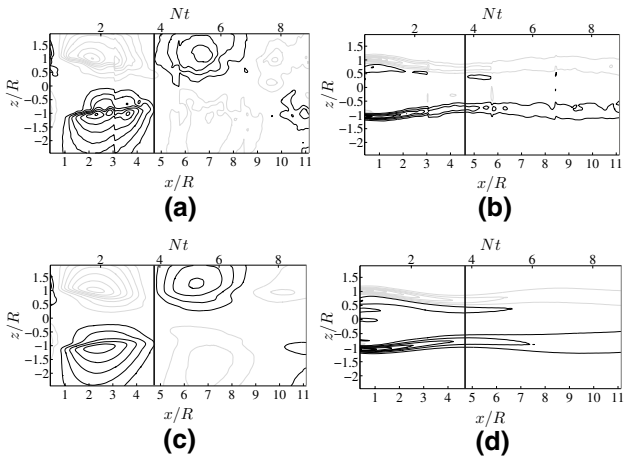

Fig. 5 Flow fields from Fr = 1.3 and Re = 2700. **a** The vertical velocity w/U of the concatenated non-oscillatory mode, with minimum contour level $|c|_{\min} = 0.02$ and contour spacing $\Delta c = 0.02$. **b** The vorticity $\omega R/U$ of the concatenated non-oscillatory mode, with $|c|_{\min} = 0.2$ and $\Delta c = 0.4$. **c** The mean vertical velocity $\overline{w}/U$, with $|c|_{\min} = 0.02$ and $\Delta c = 0.02$. **d** The mean vorticity $\overline{\omega}R/U$, with $|c|_{\min} = 0.2$ and $\Delta c = 0.6$. *Gray lines* show negative values, and the *thick vertical line* shows the *horizontal* position where the wake is maximally vertically compressed. **c** and **d** are replotted from data originally shown in Xiang et al. (2015)

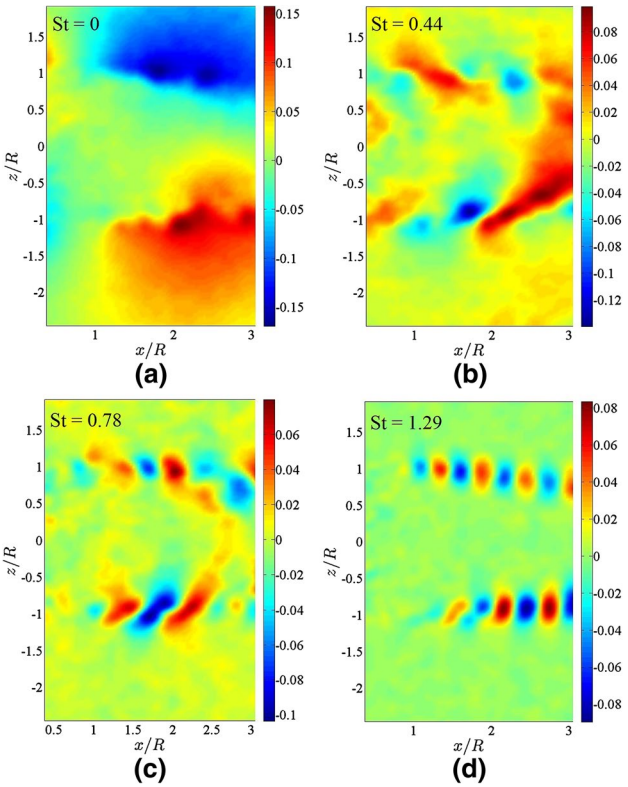

Fig. 6 Real part of w/U of (**a**) non-oscillatory mode, (**b**) oscillatory mode 1, (**c**) mode 2, and (**d**) mode 3, for Re = 2700, Fr = 1.3, at $x/R \in [0.37, 3.04]$,

mode in each sub-domain are spatially concatenated, and Fig. 5 plots the ensemble averaged vertical velocity and vorticity for this mode over 16 runs. Though the relation between the first mode and statistical mean has not been mathematically demonstrated, they seem to agree well on the lee wave characteristics. For instance, the half wavelength, marked by the vertical line at the first trough, has the same value in the non-oscillatory mode as in the ensemble average.

3.3 Temporal DMD: oscillatory modes and energy distribution

Based on the mode energy spectrum (e.g. Fig. 4), the energy contained in the first three oscillatory modes up to St ≈ 1.5 is generally larger than that in the higher-order harmonics. The vertical velocities corresponding to the four lowest St modes in Fig. 4b, which also contain much higher energy than the remaining modes, are shown in Fig. 6.

The lee wave can be clearly identified in Fig. 6a. The wavelength of the alternating-sign contours measured in Fig. 6d is about $0.6R$, which matches closely with that measured in Fig. 3b, indicating the mode around this St is associated with the initial small-scale KH mode. The St of this mode varies only a little with Re. The first oscillatory mode (Fig. 6b) corresponds to larger-scale motions which can be less organized, especially at later times. The inverse relationship between the length scale of the vortex structure in each mode and St is also clear in Fig. 6, since the length scale becomes smaller when St increases, as expected.

Since the recording time of all cases is the same, the spatial range is larger for higher Re. Therefore, here we use Re = 11,000, Fr = 2.4 as an example to study the evolution of the oscillatory modes over a relatively long distance. The energy in lower-order modes is shown in Fig. 7a for one particular x/R range, across all runs. There is no clear and persistent peak in St, nor a strict value of St that divides neighboring clusters of points in all x/R ranges and in all cases. By plotting the scaled mode energies for all x/R ranges, one finds that the point clusters not only change magnitude, but also gradually move towards smaller St with increasing distance downstream. Individual modes could be tracked to investigate their length scale and energy change with x/R. However, here in order to globally and statistically describe the energy redistribution during the wake evolution and to compare over varying Fr, boundaries are manually set at St = 0.5 and 0.9 to space the range of St evenly in [0.1, 1.3], as marked in Fig. 7a. Note that, though Fig. 7a has about the same x/R range as Fig. 6b–d, the mode structures may not be exactly the same since the Nt ranges are very different. The total energy contained in

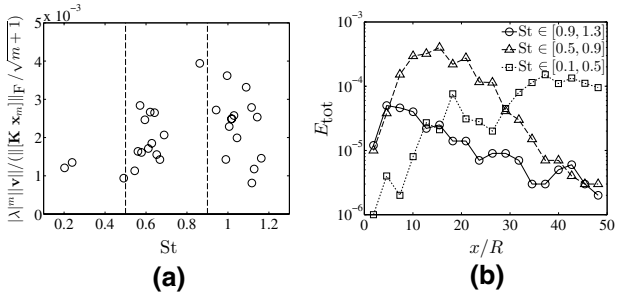

Fig. 7 DMD mode energies for Re = 11,000 and Fr = 2.4. **a** The scaled mode energies for all available runs in $x/R \in [0.55, 3.2]$, truncated at St = 1.3, with *dashed lines* separating St ranges for the E_{tot} calculation. Mode energies generally evolve toward lower St as x/R increases. **b** The mean total energy in each St range, computed from (14)

each bucket can then be calculated by ensemble-averaging the scaled energy of all modes in that St range, normalized by the mean energy of one snapshot. Hence

$$E_{\text{tot}} = \frac{(m+1)\sum_i E_i}{n_r \|[\mathbf{K}\ \mathbf{x}_m]\|_{\text{F}}^2}, \tag{14}$$

where $\{E_i\}$ is the set of mode energies with corresponding Ritz values within the given St range for all runs, and n_r is the number of runs.

The evolution of E_{tot} for the three St ranges is shown in Fig. 7b. The high St mode energy quickly decays as the initial small-scale KH rolls diffuse and intermittently merge with neighboring ones, forming medium-scale rolls of moderate St [e.g. Fig. 3 in Xiang et al. (2015); Huang and Keffer (1996)], the energy of which increases accordingly further downstream. As they further evolve, large-scale low-frequency rolls—as well as vortices that likely exist in the horizontal plane but cannot be seen by the current PIV setup—start to take over, so the energy of low St modes dominates in the far wake. This process is consistent with an inverse energy transfer in the vertical center-plane at early times. In turbulence energy can always decay towards the Kolmogorov scale (direct energy transfer), so a simultaneous transfer to larger scales implies a coexistence of direct and inverse energy transfer in the near wake, as observed in unstratified (i.e. very high Fr) porous wakes by Huang and Keffer (1996).

The stratification effects on the near-wake structures can then be investigated by comparing the energy components at varying Fr, as shown in Fig. 8 for Re = 2700 and 11,000. At Re = 2700, though not strictly monotonic, there is a general trend of increasing energy contained in all St ranges with Fr, as the experimentally resolved length scales are less suppressed by stratification at larger Fr. The evolution of different St modes for each case should proceed

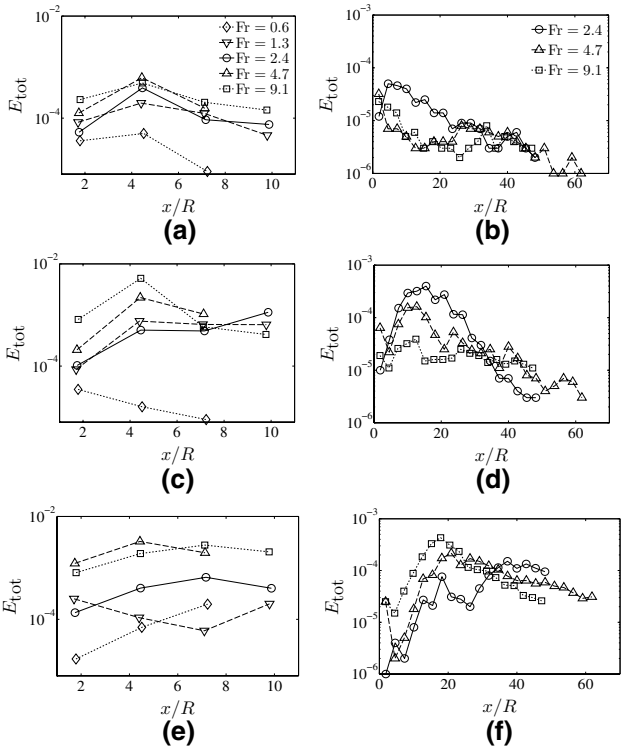

Fig. 8 The mean total energy in different St ranges for (**a**, **c**, **e**) Re = 2700 at varying Fr, and (**b**, **d**, **f**) Re = 11,000 at varying Fr. The *top row* has St ∈ [0.9, 1.3], the *middle row* has St ∈ [0.5, 0.9], and the *bottom row* has St ∈ [0.1, 0.5]

much as previously described if the effective observation distance is sufficiently long.

The Fr-dependence of the energy distribution is quite different for Re = 11,000, where the Reynolds number appears to be large enough to stimulate large-scale motions immediately in the near wake at large Fr, where buoyancy forces are comparatively weak. Most of the energy is found in low St modes at large Fr, while the energy of higher St modes remains low. If initial KH billows start at a natural frequency (small scale and therefore a high St) across all Fr, then the high energy of low Fr modes at large Fr could follow a rapid pairing of small eddies in the near wake. Meanwhile, at low Fr, strong stratification tends to keep the flow organized by constraining the vortex growth and pairing, therefore retaining more energy in smaller scales and for longer distances. The same inhibition effect of the stratification on the growth of KH billows and the pairing of the primary instability is also reported in two-layer shear flow experiments (Lawrence et al. 1991) and simulations (Smyth 2003). The reason for the different Fr-dependence of energy distribution between Re = 2700 and Re = 11,000 is not entirely clear, but a possible explanation is that the flows at these two Re are in different dynamic regimes, as

indicated by a buoyancy Reynolds number $\mathrm{Re_b} \sim \mathrm{ReFr}^2$, and discussed in our previous paper (Xiang et al. 2015).

3.4 Comparison between temporal and spatial analyses

Hydrodynamic stability theory typically distinguishes spatial analysis from temporal analysis (Schmid and Henningson 2001). In certain circumstances [e.g. Schmid (2010)], the physical interpretations of both can be equivalent for the same data set. In this study, however, though the near-wake features are temporally stable, the spatial modes can still grow unstably as the KH billows develop.

The Strouhal number in spatial analysis is computed slightly differently from (13). Since Δx is the distance between neighboring vertical slices, $\mathrm{Imag}\{\ln(\lambda_j)\}$ can be treated as the change in phase angle over a displacement Δx. We define the spatial Strouhal number to be the ratio between the characteristic length scale and the local structural length scale. Thus, it can be calculated as

$$\mathrm{St}_j^{\mathrm{s}} := \frac{R}{l_j} = \frac{k_j R}{2\pi} = \frac{\mathrm{Imag}\{\ln(\lambda_j)\}R}{2\pi\,\Delta x}, \tag{15}$$

where k_j and l_j are the wavenumber and wavelength of the jth mode, respectively. Note that $k_j u = \omega_j$, where u denotes the velocity in which the local structures move with respect to the grid, so (13) is related to (15) by

$$\mathrm{St}_j = \frac{\omega_j R}{2\pi U} = \frac{k_j u R}{2\pi U} = \frac{u}{U}\mathrm{St}_j^{\mathrm{s}}. \tag{16}$$

Since local structures actually move at a speed smaller than the towing speed—i.e., $u < U$—the Strouhal number in spatial analysis differs from that in temporal analysis by a small factor for the same flow pattern in the very near wake. However, this difference soon diminishes as the local speed with respect to the grid is quickly accelerated by the mean flow to $u \approx U$, such that $\mathrm{St}_j \approx \mathrm{St}_j^s = R/l_j$. Once this has occurred, the length scale estimated by temporal analysis is a good approximation.

A subset of the Ritz values and scaled mode energies of the spatial modes for $\mathrm{Re} = 2700$, $\mathrm{Fr} = 1.3$ is shown in Fig. 9.

The mode with $\mathrm{St}^s = 1.72$, marked by solid black dot, corresponds to a length scale of $l = R/\mathrm{St}^s = 0.58R$, which closely matches with that in Fig. 3b and the corresponding temporal analysis. This mode is, therefore, related to the KH instability and is weakly unstable in the very near wake as KH instability gradually develops. This mode slowly decays at later times, since all modes are inside the unit circle in Fig. 9b. Contours of w/U of this mode are shown in Fig. 9d. The roll-up structure can be clearly identified, and evolves through more than 3 periods in the observation window of 1.35 s. Therefore, (13) computes

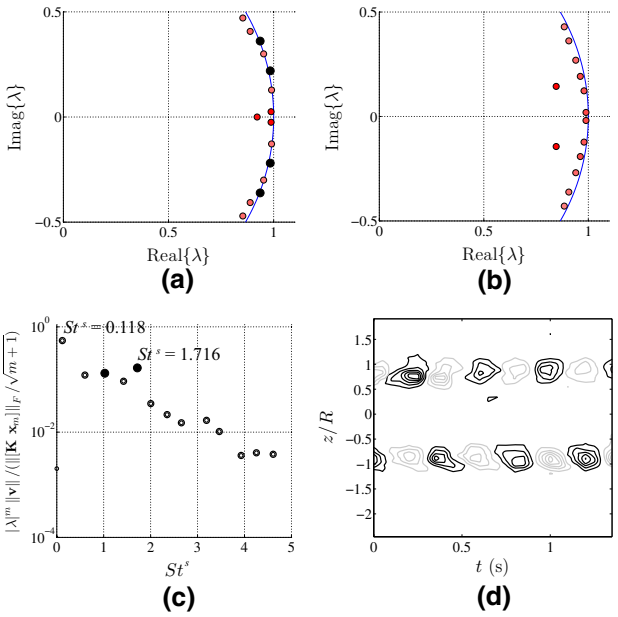

Fig. 9 Spatial DMD calculated from vertical velocity field for $\mathrm{Re} = 2700, \mathrm{Fr} = 1.3$. **a** A subset of Ritz values in $x/R \in [0.37, 3.04]$; here and in (**c**), *solid black dots* represent the mode that is weakly unstable. **b** Ritz values in $x/R \in [8.47, 11.13]$. **c** A subset of scaled mode energies for modes in $x/R \in [0.37, 3.04]$. **d** The real part of w/U of the unstable mode with $\mathrm{St}^s = 1.716$, with *black* and *gray lines*, respectively, showing contours of positive and negative vertical velocity. The minimum contour level is $|c|_{\min} = 0.006$, and the contour spacing is $\Delta c = 0.006$.

$\mathrm{St} \approx 1.3$ in temporal analysis, compared with $\mathrm{St}^s = 1.72$ in spatial analysis.

Most of energy can be found in the first 6 or 7 modes up to $\mathrm{St}^s \approx 1.9$, as can be seen in Fig. 9c. The vertical velocity fields of Mode 1, 2, 3, and 5 (the four modes with highest energy in Fig. 9c) are shown in Fig. 10.

The lee wave mode differs from other wake modes in that it moves with the grid; hence, the speed with respect to the grid is $u = 0$, and $\mathrm{St}_j = 0 \neq \mathrm{St}_j^s$. In the spatial analysis, the lee wave is recognized as a low-frequency wave mode with $\mathrm{St}^s = 0.12$ in the above example and contains more energy than other modes. Because the lee wave moves at the same speed as the grid, the vertical velocity at a given z/R is almost constant at any time t, as shown in Fig. 10a, and then its magnitude and phase changes with space. The result of $\mathrm{St}^s = 0.12 = R/l$ also agrees well with the wavelength $l/R = 2\pi\mathrm{Fr} \approx 8.2$ based on linear theory and experimental measurements (Chomaz et al. 1993; Xiang et al. 2015). In general, the spatial analysis can closely estimate the lee wave wavelength for low Fr cases, but will fail for higher Fr when the half-field of each single snapshot is too short for DMD to make a correct estimate; see Chen et al. (2012) for additional discussions on short time series. As St^s increases, the time needed for the oscillatory mode

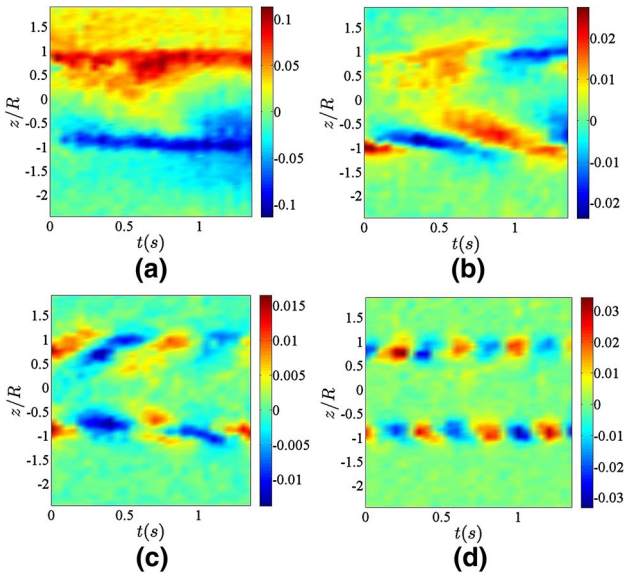

Fig. 10 Contour plots of vertical velocity fields corresponding to the four highest energy spatial modes in Fig. 9c (from *left*, Mode 1, 2, 3, 5). St increases from (**a**) to (**d**). Note the abscissa is time t

to evolve through one period decreases, as can be seen from Fig. 10b–d. This indicates a decreasing length scale with St^s, as expected since $l_j = R/\mathrm{St}_j^s$, consistent with temporal analysis.

4 Conclusion

Dynamic mode decomposition has been applied to experimental data of stratified wakes generated by a towed grid over $Nt < 10$, for a range of Froude and Reynolds numbers. The decomposition successfully captures lee wave and vortical modes of different length scales in the near wake. It also provides a means of quantifying the kinetic energy contained in different structures, thus providing insight into Froude number effects on the early time wake evolution.

In the near wake, the initial KH billows are triggered by strong shear at the wake edge. They evolve through diffusion and pairing into large-scale rolls, and DMD identifies an energy spectrum with an inverse energy transfer. One may infer that the emergence of coherent structures in the horizontal plane [e.g. Spedding (2001)] would be associated with this inverse transfer.

The energy distribution over different ranges of length scales, as identified by DMD, shows a clear Froude number dependence in the near wake. Not only do the lee wave properties rely on Fr, but also the evolution of shear modes are affected by Fr. While at $\mathrm{Re} = 2700$, a smaller Fr reduces the energy contained in all vortical modes, at $\mathrm{Re} = 11,000$ it mainly constrains the growth of KH billows and their pairing, and retains more energy in smaller scales for longer distance.

In the modal analyses, the wake structures can be described differently by temporal versus spatial DMD, though the physical interpretations are generally similar. One of the key distinctions lies in the KH mode, which is temporally neutrally stable, but spatially grows for some distance. The temporal and spatial analyses can be used to study different types of instabilities, and the current work is offered as an example of its application to a well-characterized and comparatively simple flow. The analysis suggests that DMD is a promising technique for studying the complicated modes in the near wake and for identifying the mechanisms responsible for the subsequent wave radiation and formation of pancake eddies in late wakes.

Acknowledgements We most gratefully acknowledge the support of ONR Contract N00014-14-1-0422, under the management of Dr. R. Joslin. Kevin K. Chen was supported by the Viterbi Postdoctoral Fellowship through the Viterbi School of Engineering at the University of Southern California.

References

Berkooz G, Holmes P, Lumley JL (1993) The proper orthogonal decomposition in the analysis of turbulent flows. Ann Rev Fluid Mech 25(1):539–575

Billant P (2010) Zigzag instability of vortex pairs in stratified and rotating fluids. Part 1. General stability equations. J Fluid Mech 660:354–395

Billant P, Chomaz JM (2000) Experimental evidence for a new instability of a vertical columnar vortex pair in a strongly stratified fluid. J Fluid Mech 418:167–188

Billant P, Deloncle A, Chomaz JM, Otheguy P (2010) Zigzag instability of vortex pairs in stratified and rotating fluids. Part 2. Analytical and numerical analyses. J Fluid Mech 660:396–429

Bonnier M, Eiff O (2002) Experimental investigation of the collapse of a turbulent wake in a stably stratified fluid. Phys Fluids 14(2):791–801

Chen KK, Tu JH, Rowley CW (2012) Variants of dynamic mode decomposition: boundary condition, Koopman, and Fourier analyses. J Nonlinear Sci 22(6):887–915

Chomaz JM, Bonetton P, Hopfinger EJ (1993) The structure of the near wake of a sphere moving horizontally in a stratified fluid. J Fluid Mech 254:1–21

Diamessis PJ, Gurka R, Liberzon A (2010) Spatial characterization of vortical structures and internal waves in a stratified turbulent wake using proper orthogonal decomposition. Phys Fluids 22(086):601

Diamessis PJ, Spedding GR, Domaradzki JA (2011) Similarity scaling and vorticity structure in high-Reynolds-number stably stratified turbulent wakes. J Fluid Mech 671:52–95

Gordeyev SV, Thomas FO (2000) Coherent structure in the turbulent planar jet. Part 1. Extraction of proper orthogonal decomposition eigenmodes and their self-similarity. J Fluid Mech 414:145–194

Gordeyev SV, Thomas FO (2002) Coherent structure in the turbulent planar jet. Part 2. Structural topology via POD eigenmode projection. J Fluid Mech 460:349–380

Gurka R, Liberzon A, Hetsroni G (2006) POD of vorticity fields: a method for spatial characterization of coherent structures. Int J Heat Fluid Flow 27(3):416–423

Hebert DA, de Bruyn Kops SM (2006) Predicting turbulence in flows with strong stable stratification. Phys Fluids 18(6):066602

Holmes P, Lumley JL, Berkooz G, Rowley CW (2012) Turbulence, coherent structures, dynamical systems and symmetry, 2nd edn. Cambridge University Press, Cambridge

Huang Z, Keffer JF (1996) Development of structure within the turbulent wake of a porous body. Part 1. The initial formation region. J Fluid Mech 329:103–115

Lawrence GA, Browand FK, Redekopp LG (1991) The stability of a sheared density interface. Phys Fluids 3(10):2360–2370

Lin Q, Lindberg WR, Boyer DL, Fernando HJS (1992) Stratified flow past a sphere. J Fluid Mech 240:315–354

Lumley JL (2007) Stochastic tools in turbulence. Courier Corporation

Meunier P, Diamessis PJ, Spedding GR (2006) Self-preservation in stratified momentum wakes. Phys Fluids 18:106601

Orr TS, Domaradzki JA, Spedding GR, Constantinescu GS (2015) Numerical simulations of the near wake of a sphere moving in a steady, horizontal motion through a linearly stratified fluid at $\mathrm{Re} = 1000$. Phys Fluids 27(3):035113

Riley JJ, de Bruyn Kops SM (2003) Dynamics of turbulence strongly influenced by buoyancy. Phys Fluids 15:2047–2059

Rowley CW, Mezić I, Bagheri S, Schlatter P, Henningson DS (2009) Spectral analysis of nonlinear flows. J Fluid Mech 641:115–127

Schmid PJ (2010) Dynamic mode decomposition of numerical and experimental data. J Fluid Mech 656:5–28

Schmid PJ (2011) Application of the dynamic mode decomposition to experimental data. Exp Fluids 50(4):1123–1130

Schmid PJ, Henningson DS (2001) Stability and transition in shear flows, applied mathematical sciences, vol 142. Springer, New York

Schmid PJ, Violato D, Scarano F (2012) Decomposition of time-resolved tomographic piv. Exp Fluids 52(6):1567–1579

Smyth WD (2003) Secondary Kelvin–Helmholtz instability in weakly stratified shear flow. J Fluid Mech 497:67–98

Spedding GR (1997) The evolution of initially turbulent bluff-body wakes at high internal Froude number. J Fluid Mech 337:283–301

Spedding GR (2001) Anisotropy in turbulence profiles of stratified wakes. Phys Fluids 13(8):2361–2372

Spedding GR (2002) Vertical structure in stratified wakes with high initial Froude number. J Fluid Mech 454:71–112

Spedding GR (2014) Wake signature detection. Ann Rev Fluid Mech 46:273–302

Xiang X, Madison TJ, Sellappan P, Spedding GR (2015) The turbulent wake of a towed grid in a stratified fluid. J Fluid Mech 775:149–177